The Planetary Science Journal, 6:168 (14pp), 2025 July https://doi.org/10.3847/PSJ/ade23c

Thermal-IR Observations of (152830) Dinkinesh during the Lucy Mission Flyby

Samuel L. Jackson[1], Joshua P. Emery[2], Benjamin Rozitis[1], Philip R. Christensen[3], John R. Spencer[4], Stefano Mottola[5], Victoria E. Hamilton[4], Carly J. A. Howett[6], Simone Marchi[4], Keith S. Noll[7], and Harold F. Levison[4]
[1] The Open University, Milton Keynes, Buckinghamshire, UK
[2] Northern Arizona University, Flagstaff, AZ, USA; joshua.emery@nau.edu
[3] Arizona State University, Tempe, AZ, USA
[4] Southwest Research Institute, Boulder, CO, USA
[5] Deutsches Zentrum für Luft- und Raumfahrt, Berlin, Germany
[6] Planetary Science Institute, Tucson, AZ, USA
[7] Goddard Space Flight Center, Greenbelt, MD, USA
Received 2025 January 31; revised 2025 June 4; accepted 2025 June 4; published 2025 July 17

Abstract

NASA's Lucy spacecraft flew by the main-belt asteroid (152830) Dinkinesh on 2023 November 1, providing a test of its instruments and systems prior to its encounters with the Jupiter Trojans and enabling an opportunity for scientific investigation of this asteroid. Analysis of disk-integrated radiance spectra of Dinkinesh collected by the Lucy Thermal Emission Spectrometer (L'TES) instrument during the close approach reveals a thermal inertia for Dinkinesh of 91 ± 24 J m^{-2} K^{-1} s$^{-1/2}$ and a surface roughness of $35° \pm 7°$ rms slope. These values for the thermal inertia and surface roughness are comparable to values derived for other small S-type asteroids such as (65803) Didymos. The Dinkinesh flyby also provided the opportunity to develop new techniques for extracting data when the target body does not fill the field of view of the L'TES instrument, which proved challenging for predecessors of this instrument such as OTES on OSIRIS-REx. The grain size of the regolith of Dinkinesh, estimated to be $r = 1.2^{+0.9}_{-0.6}$ mm, is below expected trends with size but is comparable to that of similarly sized asteroids that are either binaries or may have undergone rotational fission in the past. These findings imply that fine-grained materials are being preferentially retained on the primaries of multiple systems, either by cohesive forces or by redeposition after impact events on the secondaries.

Unified Astronomy Thesaurus concepts: Asteroids (72); Main belt asteroids (2036); Flyby missions (545); Infrared spectroscopy (2285)

Materials only available in the online version of record: animation

1. Introduction

NASA's Lucy mission was designed to provide the first reconnaissance of Jupiter Trojan asteroids through flyby encounters with five Trojan asteroid systems (H. F. Levison et al. 2021; C. B. Olkin et al. 2021). After launch, the team recognized that the spacecraft would pass fairly close to the small inner main-belt asteroid (152830) Dinkinesh, which was added as an opportunistic flyby target. The primary goal of the additional flyby was to test the automated terminal tracking system (C. B. Olkin et al. 2021; H. F. Levison et al. 2024). The encounter also provided the opportunity to exercise the science instruments and data processing pipelines. The encounter provided high-quality data, as well as enabling the engineering tests.

Instrumentation on board the Lucy spacecraft includes the Lucy Thermal Emission Spectrometer (L'TES), a Fourier transform infrared spectrometer provided by the Arizona State University (P. R. Christensen et al. 2024b). The flyby geometry for the Dinkinesh encounter included a fairly wide range of phase angles (120° on approach and ∼60° on departure), including the spacecraft passing through nearly zero phase (H. F. Levison et al. 2024). At the close approach distance of approximately 430 km, Dinkinesh was much smaller than the 7.3 mrad field of view (FOV) of L'TES, providing measurements of disk-integrated thermal flux at different viewing geometries.

Ground-based telescopic spectrophotometry and spectra of Dinkinesh measured prior to the Lucy spacecraft encounter revealed it to be taxonomically in the S-complex (B. T. Bolin et al. 2023; J. de León et al. 2023). From the measured absolute magnitude and average albedo for S-complex asteroids, Dinkinesh's diameter was estimated to be between 0.66 and 1.37 km (S. Mottola et al. 2023). The only similarly sized S-complex asteroids observed at high spatial resolution by spacecraft are the near-Earth asteroids (NEAs) (25143) Itokawa and (65803) Didymos (along with its moon Dimorphos). Spacecraft images of those NEAs showed abundant boulders on the surfaces, with discrete areas being more abundant in finer particulates (e.g., H. Miyamoto et al. 2007; O. Barnouin et al. 2024). Thermal inertias derived from infrared observations (700 ± 200 J m^{-2} K^{-1} s$^{-1/2}$ for Itokawa and 320 ± 70 J m^{-2} K^{-1} s$^{-1/2}$ for Didymos; T. G. Müller et al. 2014; B. Rozitis et al. 2024) are higher than measured for the Moon and large asteroids with surfaces covered in fine particulate regolith. In general, thermophysical analyses of asteroids have shown an overall decrease in thermal inertia with increasing asteroid diameter (e.g., M. Delbo et al. 2015; J. Hanuš et al. 2018; E. M. MacLennan & J. P. Emery 2022). Nevertheless, those analyses also show a wide range of

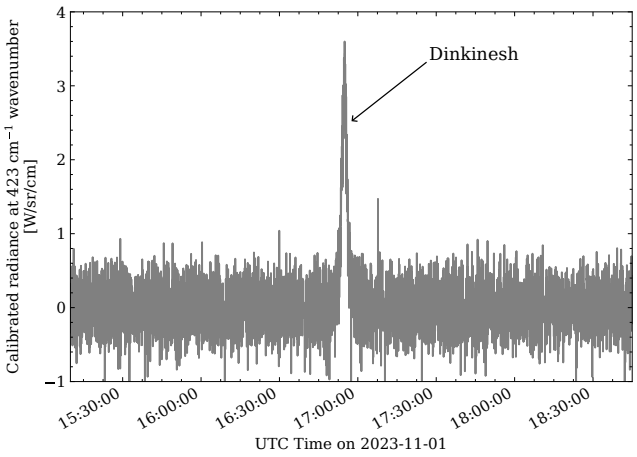

Figure 1. Calibrated spectral radiance at 423 cm^{-1} for each of the collected L'TES spectra (P. R. Christensen et al. 2024c). A clear peak is seen during the close approach of Dinkinesh.

thermal inertias for small asteroids, including some as low as the Moon (e.g., B. Rozitis et al. 2014).

In this work, we report a thermophysical analysis of Dinkinesh data to test whether the thermal properties of this small main-belt asteroid differ from small (subkilometer) S-type asteroids in the NEA population and other asteroids visited by spacecraft.

2. L'TES Observations of Dinkinesh

The L'TES instrument (see P. R. Christensen et al. 2024b for full details) is designed to aid in the characterization of the Trojan asteroids observed by the Lucy mission through the determination of their thermophysical properties. L'TES is a build-to-print mechanical copy of the OTES instrument (P. R. Christensen et al. 2018) on OSIRIS-REx (now OSIRIS-APEX; D. N. DellaGiustina et al. 2023). The primary science objective of the L'TES investigation is to determine the regolith physical properties using day and night temperature measurements, with the goal of determining the surface thermal inertia of the Trojans to within 15%. This objective is addressed using thermal infrared spectral observations between 1750 and 100 cm^{-1} wavenumber (5.7–100 μm wavelength) using a 15.2 cm diameter Cassegrain telescope. The L'TES spectral range, spectral sampling, radiometric accuracy, and spatial resolution will provide high-quality mid-infrared spectra at sufficient ground resolution to investigate the physical properties of each of the primary Trojan asteroids that Lucy will visit.

The L'TES instrument acquired data for approximately 2 hr during the Dinkinesh flyby, with interferograms acquired every 2 s with a full width at half-maximum (FWHM) FOV of 7.3 mrad (P. R. Christensen et al. 2024b). Each spectrum is tagged with a spacecraft clock (sclk; measured in seconds) value at the beginning of the scan for identification. At the closest approach distance of 430 km, the 720 m diameter asteroid, Dinkinesh, filled only 5.2% of the area of the L'TES FOV. Even with Dinkinesh only filling this small proportion of the FOV, L'TES acquired thermal infrared radiance spectra of sufficient quality to enable measurement of whole-disk temperatures, which can be used to model regolith properties such as thermal inertia, particle size, and surface roughness.

The L'TES instrument collected 6853 radiance spectra in total during the flyby, 251 of which have signal greater than the background noise (see Figure 1). The 200 radiance spectra with the highest signal (sclks 752129471–752129869) were binned into groups of 10 to increase the signal-to-noise ratio.

A complication in the analysis of the spectra obtained by L'TES is the presence of signal from the secondary in orbit around Dinkinesh, Selam, in addition to that of Dinkinesh. To establish whether Selam is within the L'TES FOV, we use the relative alignment between the L'TES FOV and that of the L'LORRI instrument (H. A. Weaver et al. 2023), which was determined using a raster scan of the Earth's Moon obtained just before Lucy's 2022 October Earth flyby (J. R. Spencer et al. 2024). The Moon was almost fully illuminated, providing a bright and relatively uniform thermal source with a radius 3.8× smaller than that of the L'TES aperture. Simultaneous L'TES and L'LORRI data during the raster scan allowed for determination of the direction and magnitude (0.45 mrad) of the boresight offset, with a precision of about 0.05 mrad.

Because the L'TES FOV is larger than the L'LORRI FOV and the boresight offset is smaller than the difference in FOV sizes, Selam is necessarily in the L'TES FOV whenever it is imaged by L'LORRI. Shortly after close approach, however, Selam leaves the L'LORRI FOV. Using the known orbital distance of Selam (3.1 km; H. F. Levison et al. 2024) and its measured separations from Dinkinesh, we computed the projected position of Selam relative to the L'TES FOV when it is outside the L'LORRI FOV. We find that Selam was also outside the L'TES FOV from about 20 s after close approach until about 215 s after close approach. This time range includes the second half of the L'TES spectra analyzed here.

When Selam is within the L'TES FOV, it contributes some thermal flux. From the dimensions of Dinkinesh (720 m diameter) and Selam (a contact binary with lobe diameters of 210 and 230 m; H. F. Levison et al. 2024), the relative contribution of Selam based purely on simple estimates of cross-sectional area would be 9% when viewed head-on and 16% when viewed side-on. However, the entire cross sections of Dinkinesh and Selam would not contribute equally because of shape, illumination, and viewing effects. For example, the thermal contribution is concentrated on the hottest parts of the surface, which would be the illuminated areas. We therefore used the images of Selam and Dinkinesh to estimate potential thermal contribution as the ratio of illuminated pixels (estimated as the pixels above some brightness threshold) and then also as the ratio of total reflected flux from those same pixels (to roughly consider viewing effects). From this analysis, we estimate that when Selam is in the L'TES FOV, it likely contributes roughly 6%–8% of the total flux, with a likely upper limit of 10%. A shape model has not been derived for Selam, and properly modeling and including its thermal flux would be both complicated and uncertain notwithstanding the additional complications that arise from thermophysical modeling of binary systems (S. L. Jackson & B. Rozitis 2024). We therefore do not explicitly consider the flux from Selam in this analysis. We note that the scale factors included in the model (described below) would adjust for excess flux, providing a first-order correction for any thermal contribution from Selam.

3. Thermophysical Model

To interpret the calibrated radiances measured by L'TES, we have used the Advanced Thermophysical Model (ATPM;

B. Rozitis & S. F. Green 2011, 2012, 2013), enabling simultaneous constraints on the thermal inertia and surface roughness of Dinkinesh. The ATPM was created to interpret thermal-IR observations of asteroids and to make predictions about the expected strength of the Yarkovsky and YORP effects on airless planetary bodies. The thermal-IR beaming effect observed in data from the Moon has been shown to be reproduced using the ATPM assuming regolith properties from Apollo in situ measurements (B. Rozitis & S. F. Green 2011).

The ATPM and models based on its implementation have been widely applied to interpret disk-integrated observations of asteroids (e.g., S. D. Wolters et al. 2011; L.-L. Yu et al. 2014; B. Rozitis 2017; D. N. DellaGiustina et al. 2019; B. Rozitis et al. 2024). The ATPM has also been used to interpret disk-resolved IR data of the OSIRIS-REx target (101955) Bennu (B. Rozitis et al. 2020, 2022; A. J. Ryan et al. 2024) collected by the OTES instrument (P. R. Christensen et al. 2018). For full details of the ATPM, the reader is directed to B. Rozitis & S. F. Green (2011, 2012, 2013), while the principal details of the model are summarized here.

Given a set of input parameters (Bond albedo, thermal inertia, asteroid shape, and spin state), the ATPM calculates the asteroid surface and subsurface temperature distribution. These temperatures are computed by solving the one-dimensional heat diffusion equation (Equation (1)) for each facet on the input shape model for each time step during a rotation of the shape, using two boundary conditions. The facets are constructed from the shape model. The shape model comprises a list of vertex coordinates and lines defining each "facet" by the IDs of three vertices that define a triangular surface (vertices are ordered counterclockwise to provide a surface normal vector facing outward).

The first of these boundary conditions is the balance of solar input flux, scattered sunlight from interfacing facets, mutual heating between facets, emitted energy through thermal emission, and heat conduction into/out of the subsurface (Equation (2)) at the surface of each facet. The second boundary condition mandates that the amplitude of temperature variations tends to zero with increasing depth below the surface (Equation (3)):

$$\frac{dT}{dt} = \frac{k}{\rho C_P}\frac{d^2T}{dx^2}, \tag{1}$$

$$(1 - A_B)([1 - S(t)]\psi(t)F_{SUN} + F_{SCAT}) + F_{RAD} + k\left(\frac{dT}{dx}\right)_{x=0} - \varepsilon\sigma T^4 = 0, \tag{2}$$

$$\left(\frac{\partial T}{\partial x}\right)_{x\to\infty} \to 0. \tag{3}$$

In Equation (1), the parameters are defined as follows: T is temperature, t is time, k is thermal conductivity, ρ is density, C_P is the specific heat capacity, and x is depth. In Equation (2), the parameters are defined as follows: A_B is the bolometric Bond albedo, $S(t)$ calculates the shadowing of each facet, $\psi(t)$ represents the cosine of the illumination angle for each facet, F_{SUN} is the integrated solar flux at the distance of the asteroid from the Sun, F_{SCAT} represents multiple scattering of incident sunlight, F_{RAD} represents self-heating from interfacing shape facets, ε is the bolometric emissivity, and σ is the Stefan–Boltzmann constant.

Surface roughness at scales smaller than the shape model facets is explicitly included in the ATPM. To model the effects of surface roughness, each facet on the shape model is replaced with a hemispherical crater comprising 100 subfacets, with geometries at each time step computed relative to the shape model facet normal at that time step. The temperature of each of these subfacets is calculated in the same way as the original shape facets as detailed previously (these subfacets are still much larger than the scale of the thermal skin depth, and so one-dimensional heat conduction can still be applied).

In total, we calculate the surface and subsurface temperature distribution for each shape facet and roughness subfacet over 650 time steps, with 56 depth steps used to model the heat flow into and out of the subsurface. For this shape model with 5186 shape facets (and therefore 518,600 total roughness subfacets), this results in the calculation of over 19×10^9 temperature values for each run of the thermal model. The model is then run for 100 thermal inertia values, giving a total of over 1.9×10^{12} temperatures calculated by the ATPM across this analysis (of which 34×10^9 are surface temperatures of the shape facets and roughness subfacets).

The thermal flux emitted by each facet toward the observer at each time step is computed by the Planck function from the modeled surface temperature, multiplied by the projected area of the facet (relative to the observer) and the emissivity, and divided by the square of the distance to the observer (Equation (4)),

$$F_{MOD,i}(\Gamma, \lambda, t) = B(\lambda, T_i(\Gamma, t))\varepsilon(\lambda)\frac{a_i}{\Delta^2}\cos(e), \tag{4}$$

where $F_{MOD,i}(\Gamma, \lambda, t)$ is the facet flux, $B(\lambda, T_i(\Gamma, t))$ is the Planck function, $\varepsilon(\lambda)$ is the spectral emissivity, a_i is the facet surface area, Δ is the distance to the observer from the facet, and e is the emission angle (B. Rozitis et al. 2024). The fluxes for facets visible to the observer are summed to get the disk-integrated flux at each time step. This computation is made for each trial value of the the thermal inertia. The same process is also applied to the roughness subfacets to find the "fully rough" thermal flux, giving us the "fully smooth" and "fully rough" fluxes. The roughness fraction can then be varied as a free parameter, f_R, which controls the fractional coverage of rough surfaces across the modeled asteroid, which is manifested through a weighted linear combination of smooth and rough model fluxes. The total flux can therefore be described as per Equation (5),

$$F(\Gamma, f_R, \lambda, t) = \sum_{i=1}^{N} v_i\left(t)((1 - f_R)F_{MOD,\,i}(\Gamma, \lambda, t) + f_R\sum_{j=1}^{M} v_{ij}(t)F_{MOD,\,ij}(\Gamma, \lambda, t)\right), \tag{5}$$

where $F(\Gamma, f_R, \lambda, t)$ is the total flux, v_i is the fractional visibility of facet i, v_{ij} is the fractional visibility of roughness subfacet j of facet i, and f_R is the roughness fraction. For example, for a model with a roughness fraction of 0.3 (i.e., 30% of the surface is "rough"), the model output flux will be a combination of 30% of the "fully rough" model flux plus 70% of the "fully smooth" model flux. This roughness fraction can then be interpreted in terms of rms slope by rms Slope [degrees] $=49\sqrt{f_R}$ (B. Rozitis & S. F. Green 2011).

Table 1
Summary of the Observational Geometries over the Duration of the 10 Binned Spectra Selected for Analysis with the ATPM

Spectrum No.	sclk (s)	Range (km)	Lucy-Centered Ecl. Lon. (deg)	Lucy-Centered Ecl. Lat. (deg)	Phase Angle (deg)
1	752129540	536.9	134.1	8.5	−67.6
2	752129560	486.1	142.4	7.8	−59.3
3	752129580	448.4	152.4	6.7	−49.3
4	752129600	427.0	163.8	5.1	−37.9
5	752129620	422.7	175.9	3.3	−25.7
6	752129640	436.4	187.5	1.5	−13.9
7	752129660	467.8	197.9	−0.2	−3.5
8	752129680	513.6	206.8	−1.7	5.7
9	752129700	570.3	214.3	−3.0	13.3
10	752129720	634.3	220.3	−3.9	19.3

Note. The heliocentric position of Dinkinesh is held fixed at $\lambda_{\mathrm{Hel.}} = 201.^{\circ}38$, $\beta_{\mathrm{Hel.}} = 0.^{\circ}00011$, 2.264 au during the simulations due to the negligible changes over the close approach, simplifying the computation of temperature lookup tables. The "sclk" column corresponds to the average sclk value of the 10 spectra that are averaged to provide the binned spectra.

4. Analysis of L'TES Spectra

The first step in the ATPM analysis was to convert the L'TES measurements from radiance units to flux units using an FWHM value for the L'TES FOV of 7.3 mrad (P. R. Christensen et al. 2024b). The averaged spectra (see Section 2) were filtered to select the 10 with the best signal for analysis with the ATPM, and the rest were discarded to avoid fitting such a sensitive model to data with low signal-to-noise. The observational geometries of these 10 spectra are summarized in Table 1, and the binned spectra can be seen in Figure A1.

The heliocentric ecliptic coordinates and the Lucy-centered ecliptic coordinates of Dinkinesh were obtained from the JPL Horizons ephemeris system for the average times of the binned spectra. The accuracy of the JPL Horizons ephemerides are comparable to the reconstructed trajectories, and any differences will have an effect lower than other systematics discussed later in this work. Due to the short timescale of the flyby (particularly the 200 s of measurements we analyze in this work), the heliocentric ecliptic coordinates of Dinkinesh were held fixed at the average value across the spectra to simplify computation (this requires only one run of the thermal model) as the differences in global temperatures calculated at the times of each spectrum are negligible (i.e., only changing observation geometry is considered to alter the spectra observed by L'TES).

The shape (v2.02) and spin state derived by F. Preusker et al. (2024) are provided as input into the ATPM, with ecliptic pole coordinates of $\lambda = 95.^{\circ}53$ and $\beta = -87.^{\circ}05$ and a rotation period $P_{\mathrm{ROT}} = 3.737$ hr. For this work, the shape model was resampled from 126,627 facets to 5186 facets using the quadric edge collapse decimation tool in MeshLab (M. Garland & P. S. Heckbert 1997; P. Cignoni et al. 2008) to prevent excessive computation for roughness facets (and to limit memory consumption). The ATPM analysis is largely sensitive to global shape effects instead of small-scale topography and includes smaller-scale roughness through hemispherical craters as mentioned in Section 3. The effect of small-scale topography would perhaps be more significant for observations where a larger fraction or all of the FOV is filled, such as those during the upcoming Trojan asteroid flybys.

From photometric modeling of flyby imagery, a Bond albedo was derived ($A_{\mathrm{B,EFF}} = 0.114$; S. Mottola et al. 2024). This Bond albedo, however, is the effective rough-surface Bond albedo. It must therefore be transformed using Equation (6) (S. D. Wolters et al. 2011) to the "smooth-surface Bond albedo" that the ATPM requires as input. Using an assumed roughness fraction of $f_R = 0.5$ (a good approximation for most asteroids), we derive a smooth-surface Bond albedo of $A_{\mathrm{B}} = 0.15$ to input into the ATPM. The effect of this assumed roughness fraction for the conversion is discussed further in this section:

$$A_{\mathrm{B,EFF}} = f_R \frac{A_{\mathrm{B}}}{2 - A_{\mathrm{B}}} + (1 - f_R) A_{\mathrm{B}}. \quad (6)$$

The ATPM produces temperatures over 650 time steps covering a full rotation of Dinkinesh. However, as the L'TES observations are not resolved images, the time step corresponding to the L'TES observations was determined through simulation of the shape over the observations and visual comparison to L'LORRI images taken simultaneously. An example of the match between the simulated shape and the L'LORRI observations can be seen in Figure 2. There is some uncertainty in which the model time step matches each L'TES observation, and so when generating simulated fluxes from the ATPM, we average over 10 time steps either side of the best estimate and output the standard deviation of these spectra as the uncertainty on the model spectra.

To find the optimal parameters that describe the observed data, we adopt a "brute force" approach; i.e., the fluxes are calculated across all thermal inertia trial values (from 0 to 1000 J m^{-2} K^{-1} s$^{-1/2}$ in steps of 10 J m^{-2} K^{-1} s$^{-1/2}$) and all trial values for the surface roughness (from 0° to 70° rms slope in steps of 1°). An additional scale factor is included as a free parameter (from 0 to 2 in steps of 0.001) for each binned spectrum that allows for magnitude shifts in the model fluxes to match the data, allowing for uncharacterized systematics such as instrumental effects, uncertainty in the size of Dinkinesh, and variable contributions from Selam to be accounted for. The χ^2 between the model fluxes and the data are calculated for all trial parameter combinations. Acceptable parameter values are defined at the 3σ level as any combination that provided a χ^2 value within $\Delta\chi^2 = 14.2$ of the minimum value (W. H. Press et al. 2002, p. 697). The fitted parameter values and their uncertainties are then taken as the mean and standard deviation of the acceptable parameters. We then calculate the total χ^2 across all 10 spectra for the range of thermal inertia and roughness trial values (Figure 3). The parameters are derived as $\Gamma = 91 \pm 24$ J m^{-2} K^{-1} s$^{-1/2}$ and rms slope $= 35° \pm 7°$ with $\chi^2_\nu = 1.41$. The ATPM fits to the averaged spectra are shown in Figure A1, along with single-temperature blackbody fits for comparison.

It is noted that the fitted rms slope of 35° corresponds to a roughness fraction of $f_R = 0.5$, which is the same as the roughness fraction assumed for the conversion between rough-surface and smooth-surface Bond albedo. To verify that our modeling process was not just converging back onto this initial assumption, we remodeled the data using initial f_R values for the conversion of 0.3 and 0.7 (which correspond to A_{B} of 0.132 and 0.167), providing bracketing solutions around the original assumed value. The modeling results using these bracketed values provided no change in the derived roughness of Dinkinesh, indicating that the modeling

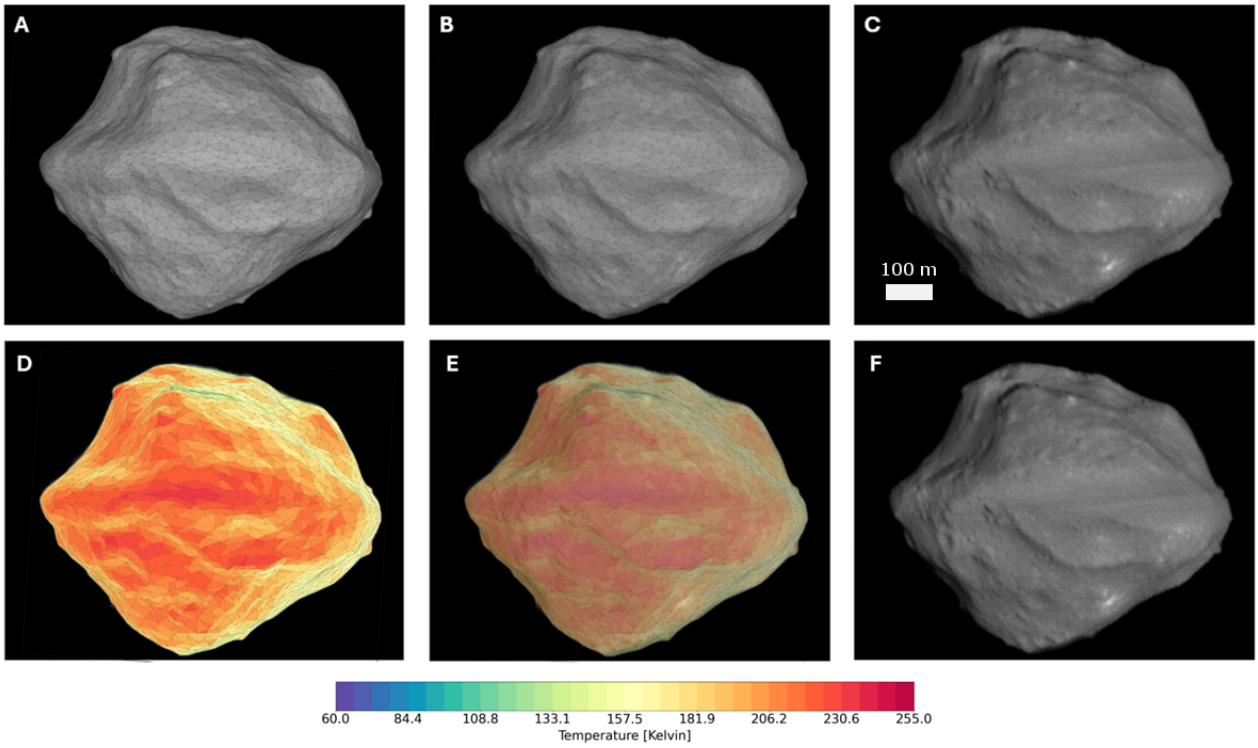

Figure 2. Example comparison of the simulated shape of Dinkinesh overlaid on a L'LORRI image, used to determine the time step/rotation angle of Dinkinesh corresponding to the L'TES observations taken simultaneously. Panels (A)–(C): decreasing opacity of the simulated shape at the best time step from left to right. Panels (D)–(F): the same as (A)–(C) but with a simulated temperature map for a thermal inertia of 90 J m^{-2} K^{-1} $s^{-1/2}$.

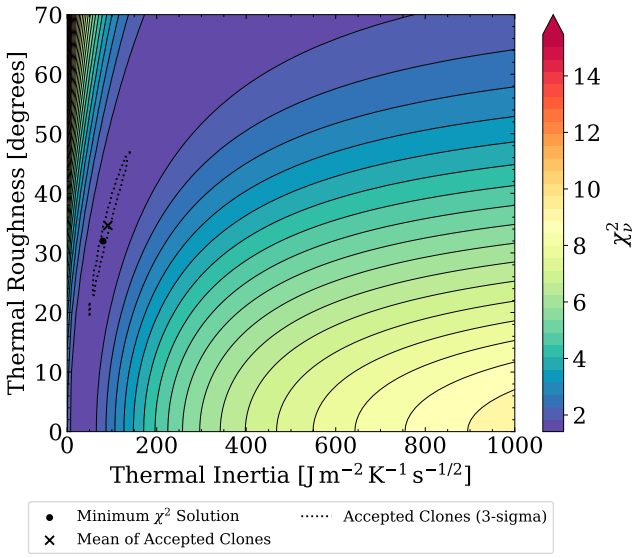

Figure 3. χ^2 contour plane for thermal inertia vs. roughness. The color bar indicates the reduced χ^2 value across the 10 spectra. The black circle denotes the minimum χ^2 solution. The dotted contour denotes accepted 3σ solutions within $\Delta\chi^2 = 14.2$ of the minimum χ^2. The black cross denotes the mean of the accepted 3σ solutions (i.e., the final parameter estimates).

and fitting process is not fitting to the initial assumption. Additionally, the derived thermal inertias and scale factors shifted by small amounts, well within the derived uncertainties in the original analysis. We therefore do not consider the assumption of a thermal roughness for the rough-surface to smooth-surface Bond albedo conversion to provide any significant bias within these results.

In Figure 4(a) (red shaded region), we show the scale factors fit to the spectra as a function of observation phase angle; in Figure 4(b) (red line), we show the single-temperature blackbody temperatures fit to both the L'TES data and our best-fit model; and in Figure 4(c) (red line), we show the reduced χ^2 statistic values for the best-fit model compared to the L'TES data. These curves suggest that our model is not providing a complete understanding of this system, particularly at higher phase angles. The misfits at high phase angles could be a result of contribution from Selam or the presence of shape facets unseen in L'LORRI data that are not able to be accurately modeled (both discussed further in Section 5).

An interesting alternative possibility to consider is surface heterogeneity. Panel (C) of Figure 2 shows a bright spot on the surface of Dinkinesh, suggesting some heterogeneity in the visible albedo. There is also some evidence of heterogeneity in the visible wavelength spectral slope and/or 1 μm band depth on Dinkinesh from ground-based spectroscopy (B. T. Bolin et al. 2023). Therefore, we also assess whether there is evidence of heterogeneity on the surface of Dinkinesh in the thermal-IR wavelength range that is apparent in the L'TES data.

For the reanalysis of the data with a heterogeneous surface, we do not leave the roughness as a free parameter, as fitting to the individual spectra does not allow for a reliable constraint on roughness, and therefore it is held fixed at the homogeneous model best-fit roughness, 35° ± 7°. We allow the thermal inertia and scale factors to be fit individually to each spectrum. The ATPM fits to the averaged spectra are shown in Figure A2, along with single-temperature blackbody fits for comparison. The thermal inertia values fitted to the spectra are plotted against phase angle in Figure 5. Ignoring the first two (high phase angle) points, some systematic trend in the data is suggested, but this trend is not

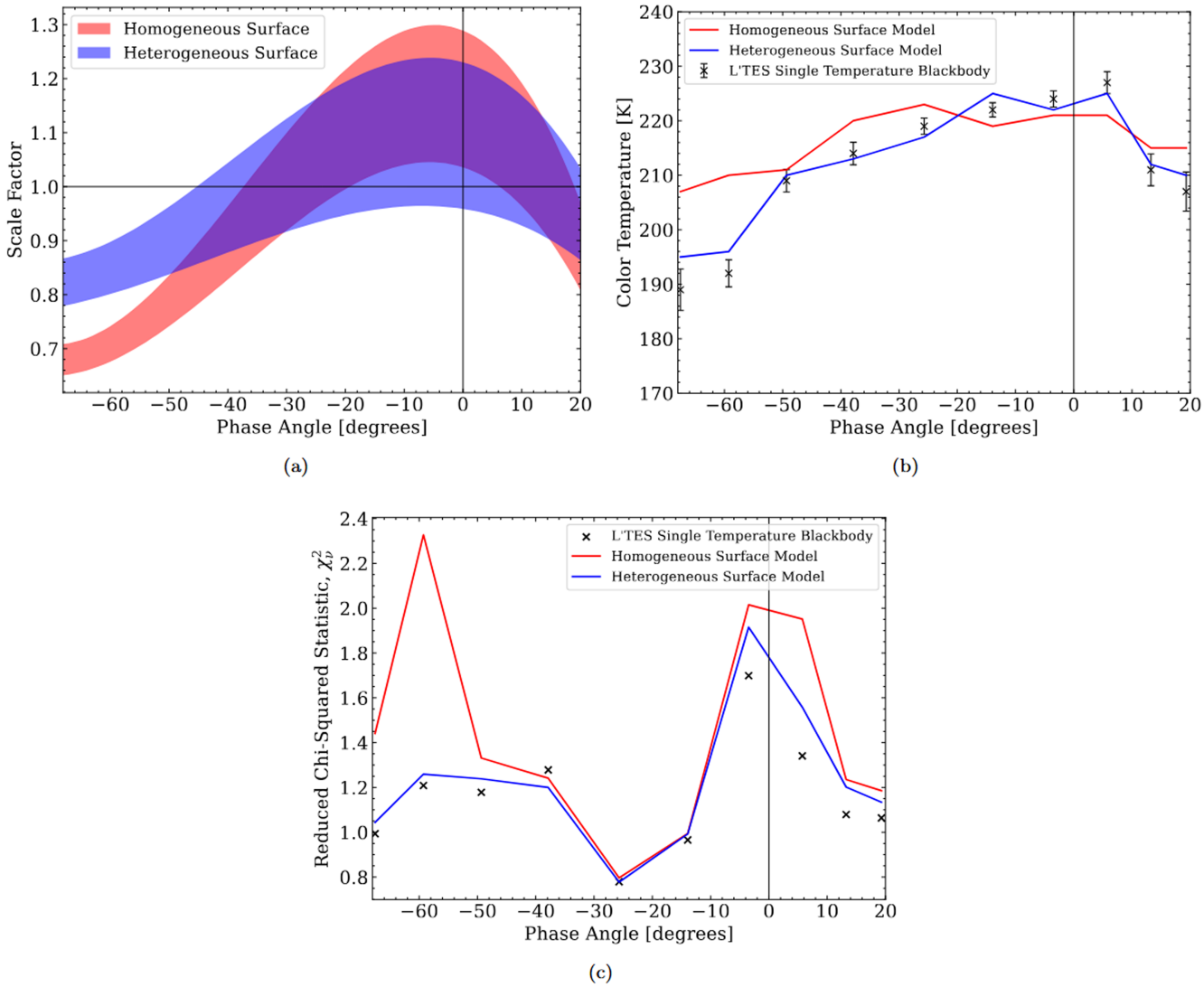

Figure 4. (a) Scale factors fitted to each spectrum plotted with phase angle for the homogeneous model (red shaded region) and the heterogeneous model (blue shaded region). (b) Single-temperature blackbody temperatures fitted to the L'TES spectra (black crosses), the best-fit homogeneous surface ATPM spectra (red line), and the best-fit heterogeneous surface ATPM spectra (blue line). (c) Reduced χ^2 statistic values for the single-temperature blackbody fits (black crosses), best-fit homogeneous surface ATPM spectra (red line), and best-fit heterogeneous surface ATPM spectra (blue line).

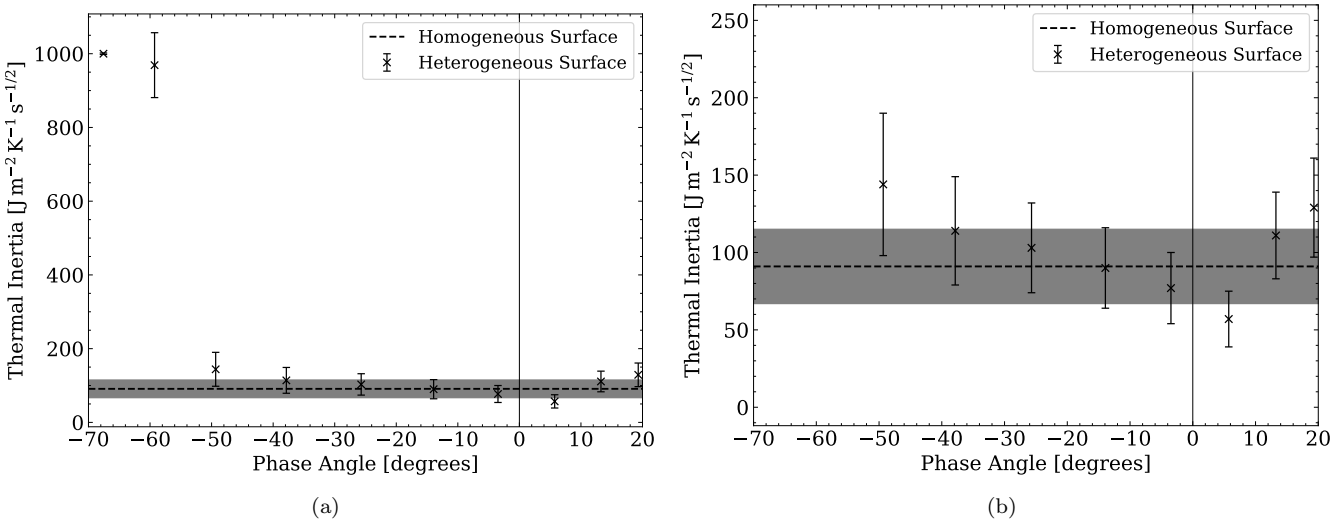

Figure 5. Thermal inertia values derived from the individual L'TES spectra varying with phase angle. Tentative, but not significant, evidence of surface heterogeneity is present in these data. (a) All measurements. (b) *Y*-axis rescaled to exclude the two initial values and show a trend in the eight remaining values.

Table 2
Thermal Inertia Values Derived for Subkilometer Asteroids Visited by Spacecraft

Asteroid	Thermal Inertia ($J\,m^{-2}\,K^{-1}\,s^{-1/2}$)	Roughness (deg rms slope)	r (au)	Scaled Thermal Inertia ($J\,m^{-2}\,K^{-1}\,s^{-1/2}$)	References
(152830) Dinkinesh	1 ± 24	35 ± 7	2.26	168 ± 44	(1)
(65803) Didymos	320 ± 70	40 ± 3	1.11	346 ± 76	(2)
(276049) 2002 CE26	⋯	36 ± 10	⋯	255^{+165}_{-105}	(3)
(175706) 1996 FG3	142 ± 6	27 ± 12	1.22	165 ± 7	(4)
(1862) Apollo	140 ± 120	38 ± 10	1.10	151 ± 128	(5)
(25143) Itokawa	700 ± 200	41	1.06	731 ± 209	(6)
(433) Eros	$100 - 200$	38 ± 7	1.62	$144 - 287$	(7)
(101955) Bennu	300 ± 30	40 ± 2	1.04	⋯	(8)
(162173) Ryugu	225 ± 45	47 ± 5	1.06	⋯	(9)

Note. The scaled thermal inertia values are scaled to represent the expected values at 1 au. Thermal inertia values for Bennu and Ryugu are not scaled due to the presence of highly porous boulders (D. N. DellaGiustina et al. 2019; S. Sugita et al. 2019), which are not expected to experience temperature-dependent changes in thermal inertia (e.g., B. Rozitis et al. 2020). The value for the scaled thermal inertia of (276049) 2002 CE26 was derived from a fit to the heliocentric distance variations in thermal inertia measured for this object.

References: (1) This work; (2) B. Rozitis et al. (2024); (3) B. Rozitis et al. (2018); (4) S. L. Jackson & B. Rozitis (2024); (5) B. Rozitis et al. (2013); (6) T. G. Müller et al. (2014); (7) M. M. Müller (2007); (8) B. Rozitis et al. (2020); (9) Y. Shimaki et al. (2020).

significant compared to the uncertainties on the individual fits or the homogeneous model fit (gray box and dashed line). The initial two spectra provide significantly higher values for the thermal inertia compared to the rest, which could be a result of low signal-to-noise and also the increased proportion of the shadowed region of the shape in the FOV that is not as well constrained by the shape modeling process. In Figure 4(a) (blue shaded region), we show the scale factors of the individual fits overplotted with those from the homogeneous fits (x-positions offset for clarity). A marginal improvement is made to these scale factors by the heterogeneous analysis. The blackbody color temperatures of the model spectra also better match those of the data, as seen in Figure 4(b) (blue line). The χ^2 values are also improved, as shown in Figure 4(c) (blue line). We must offer the caveat that this analysis may be approaching the realm of overfitting of these data, and so we do not claim that Dinkinesh has a heterogeneous surface. Instead, we provide this analysis for context in the overall picture of the surface of Dinkinesh.

5. Discussion

5.1. Thermal Inertia

The derived global average thermal inertia from this analysis of $91 \pm 24\,J\,m^{-2}\,K^{-1}\,s^{-1/2}$ indicates the presence of small particulates on the surface of Dinkinesh. Although relatively low thermal inertia measurements ($\lesssim$ a few hundred $J\,m^{-2}\,K^{-1}\,s^{-1/2}$) can also be present for surfaces with porous boulders (B. Rozitis et al. 2020), the imaging data from the L'LORRI instrument (for example, in Figure 2(C)) do not indicate a global presence of large boulders as was seen on (101955) Bennu and (162173) Ryugu. The pixel scale of the highest-resolution image was 2.1 m (and the pixel scale of the image in Figure 2 was 2.3 m), so boulders >10 or 15 m would have been readily resolved. The thermal inertia of Dinkinesh is comparable to similar bodies that have been visited by spacecraft after accounting for heliocentric distance effects on thermal inertia (B. Rozitis et al. 2018).

To assess the consistency of this thermal inertia measurement with those of previously characterized small binary systems, we compare the results to those obtained with the ATPM for (65803) Didymos (B. Rozitis et al. 2024), (276049) 2002 CE26 (B. Rozitis et al. 2018), (175706) 1996 FG3 (S. D. Wolters et al. 2011; S. L. Jackson & B. Rozitis 2024), and (1862) Apollo (B. Rozitis et al. 2013). The thermal inertia values derived for these objects in the literature and the thermal inertia values scaled to a heliocentric distance of 1 au are presented in Table 2. We can see that the values derived for Dinkinesh in this work are largely consistent with other small binary systems in the literature within their respective uncertainties. The thermal inertia of Dinkinesh has a slightly worse correspondence with that of Didymos, although the uncertainties still overlap at the 2σ level. The thermal inertia derived for Dinkinesh is also comparable to that of (433) Eros, despite the significant size difference between these objects and the difference in processes that break down regolith on their surfaces. These measurements of Dinkinesh are also consistent with the work of F. Marchis et al. (2012), who found thermal inertias $\lesssim 100\,J\,m^{-2}\,K^{-1}\,s^{-1/2}$ for (albeit large, $D > 130$ km) main-belt binaries. The similarity of the thermal inertia values between large main-belt binaries and a small main-belt binary such as Dinkinesh implies that regolith processes during binary formation and evolution are comparable at these different scales.

Understanding why these binaries typically have low thermal inertia values poses interesting questions. A binary-forming object without surface cohesion would see small and large regolith grains lost equally during a rotational fission event. However, smaller grains may be preferentially retained on a surface with cohesion as cohesive forces will dominate at this size scale (D. J. Scheeres et al. 2010). The low thermal inertia values derived in this work and previous studies of binaries suggests that fine-grained material is preferentially retained during rotational fission in these systems by van der Waals forces.

An alternative explanation for these low thermal inertia values may lie in the dynamics of impacts into the secondaries of these objects. NASA's recent Double Asteroid Redirection Test mission (A. S. Rivkin et al. 2021; N. L. Chabot et al. 2024) impacted the secondary of the (65803) Didymos system, potentially redepositing material from the secondary onto the surfaces of both components (Z. Gray et al. 2024). Similar dynamics for smaller-scale impacts could cause the redeposition of fines from a secondary back onto a primary body (which dominates the thermal flux we see in disk-integrated observations), creating a fine blanket of material on the surface

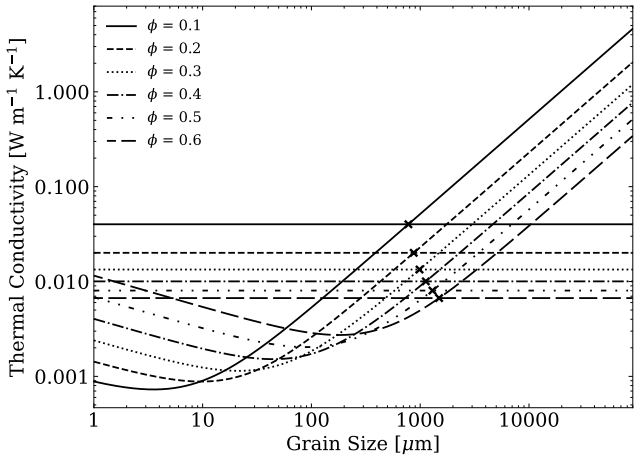

Figure 6. Grain size estimation for varying volume filling factors. Horizontal lines represent the thermal conductivities calculated from the nominal thermal inertia value for Dinkinesh of $\Gamma = 91\ \mathrm{J\ m^{-2}\ K^{-1}\ s^{-1/2}}$. The curves describe the thermal conductivity model (assuming parameters for stony meteorites) as a function of regolith grain size. The intersection between the thermal conductivity model and the derived thermal conductivity provides the estimate of the grain size for that volume filling factor.

and subsequently lowering the average thermal inertia. ESA's Hera mission (P. Michel et al. 2022) will revisit the Didymos system and be able to obtain resolved thermal imaging of the surfaces of both components, potentially aiding in our understanding of the exchange of material between components of a binary asteroid system.

5.2. Grain Size Estimation

Measurements of thermal inertia can be used to derive the characteristic regolith grain size using a model for the thermal conductivity (e.g., B. Gundlach & J. Blum 2013, 2015; V. Alí-Lagoa et al. 2014). A summary of the method is provided here, but for full details of the model, see B. Gundlach & J. Blum (2013). Note that in this work, we denote the thermal conductivity with the symbol k, whereas in B. Gundlach & J. Blum (2013), they use λ. The thermal conductivity of an asteroid can be derived from the thermal inertia as

$$k = \frac{\Gamma^2}{\phi \rho C}, \tag{7}$$

where Γ is the thermal inertia, ϕ is the volume filling factor, ρ is the regolith material density (not equivalent to the bulk density of Dinkinesh as a whole), and C is the heat capacity of the regolith material. To estimate the thermal conductivity, we used values for the material density and heat capacity of L-chondrite meteorites (C. P. Opeil et al. 2010). Ordinary chondrites provide an analog for the material present on the surface of Dinkinesh as they match the expected composition of S-type asteroids (T. Nakamura et al. 2011). The volume filling factor is not known, and so we allow this parameter to vary from $\phi = 0.1$ (only possible for small particles in low-g environments) to $\phi = 0.6$ (approaching maximum packing density for equal-sized spheres) in steps of $\Delta\phi = 0.1$. The derived values of the thermal conductivity for the different volume filling factors are shown by the horizontal lines in Figure 6 for the nominal Dinkinesh thermal inertia of $\Gamma = 91\ \mathrm{J\ m^{-2}\ K^{-1}\ s^{-1/2}}$. These values range from 0.007 to $0.040\ \mathrm{W\ m^{-1}\ K^{-1}}$ across the different volume filling factors.

Table 3
Summary of Material Properties Input into the Thermal Conductivity Model

Physical Property	Value	Unit	References
μ	0.25	⋯	(1)
E	$(7.8 \pm 1.9) \times 10^{10}$	Pa	(1)
T	211 ± 12	K	(2)
$\gamma(T)$	$6.67 \times 10^{-5}\ T$ [K]	J m^{-2}	(3)
k_{solid}	2.18	W m^{-1} K^{-1}	(4)
ρ	3620	kg m^{-3}	(4)
C	570	J kg^{-1} K^{-1}	(4)
ε	0.9	⋯	⋯
f_1	$(5.18 \pm 3.45) \times 10^2$	⋯	(5)
f_2	5.26 ± 0.94	⋯	(5)
χ	0.41 ± 0.02	⋯	(6)
e_1	1.34 ± 0.01	⋯	(6)

Notes. μ: Poisson's ratio. E: Young's modulus. T: average of single-temperature blackbody fits. $\gamma(T)$: specific surface energy. $k_{\mathrm{solid}}(T)$: heat conductivity of the solid material. ρ: density of the solid material. C: heat capacity of the solid material. ε: emissivity of the material. f_1, f_2, χ, e_1: constants derived by B. Gundlach & J. Blum (2012, 2013).
References: (1) R. A. Schultz (1995); (2) this work; (3) B. Gundlach & J. Blum (2012); (4) C. P. Opeil et al. (2010); (5) B. Gundlach & J. Blum (2012); (6) B. Gundlach & J. Blum (2013).

To derive the grain size of the regolith on Dinkinesh, we then apply a model for the thermal behavior of granular materials in a vacuum (B. Gundlach & J. Blum 2012) describing the relationship between thermal conductivity and grain size (Equation (8)) using a set of parameters assumed for stony meteorites summarized in Table 3 (B. Gundlach & J. Blum 2013):

$$k(r, T, \phi) = k_{\mathrm{solid}}(T)\left[\frac{9\pi}{4}\frac{1-\mu^2}{E}\frac{\gamma(T)}{r}\right]^{1/3} (f_1 \exp[f_2 \phi])\chi + 8\sigma\varepsilon T^3 e_1 \frac{1-\phi}{\phi} r. \tag{8}$$

To calculate the grain size of the regolith of Dinkinesh, we calculate the intersection points between the thermal conductivity model (Equation (8)) and the calculated conductivity (Equation (7)) for each volume filling factor, ϕ (see Figure 6 for an example for the nominal thermal inertia value case). For those properties that have reported uncertainties, including the thermal inertia derived in this work, we resample the parameters 1000 times using Gaussian distributions centered at the nominal values and with standard deviations equal to the reported uncertainties. We then calculate the grain sizes across the different volume filling factors for each resampling. The grain size is then reported as the mean of these values across all resamplings and volume filling factors, $r = 1.2^{+0.9}_{-0.6}$ mm, with the 16th and 84th percentiles of the distribution describing the upper and lower 1σ bounds.

In Figure 7, we plot grain sizes versus gravitational acceleration for a number of bodies from B. Gundlach & J. Blum (2013; excluding those marked as IRAS observed in their work, due to the systematic offset observed with those data). The black lines in Figure 7 are the mathematical models fit to the data by B. Gundlach & J. Blum (2013). In addition, we plot the grain size derived for Dinkinesh. The value for Dinkinesh does not agree well with the trends observed in the data but forms a cluster of points that do

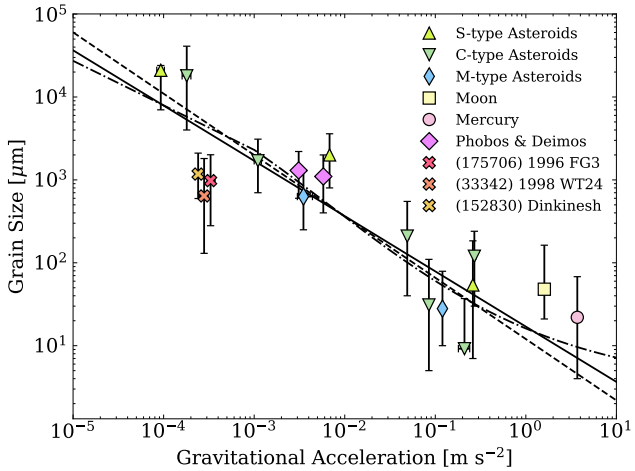

Figure 7. Grain sizes for a variety of solar system objects as a function of gravitational acceleration from B. Gundlach & J. Blum (2013), excluding objects observed with IRAS (which were systematically offset). The black lines are the mathematical models fit to the non-IRAS data by B. Gundlach & J. Blum (2013). Dinkinesh does not overlap with the fits to the rest of the asteroids, along with the C-type binary (175706) 1996 FG3 and the M-type asteroid (33342) 1998 WT24.

not fit the trends, joining the binary asteroid (175706) 1996 FG3 and the NEA (33342) 1998 WT24. 1998 WT24 is expected to have been spinning at or close to the spin-fission limit ~75 kyr ago from derivation of its predicted (but not yet detected) YORP spin-down (M. W. Busch et al. 2008). This object may therefore have lost material through rotational fission in its past in a similar fashion to the formation of the secondaries of Dinkinesh and 1996 FG3.

The similar grain sizes of these objects suggest that cohesive forces are the dominant driver behind the low thermal inertia values measured for binary asteroids such as Dinkinesh and 1996 FG3, and that similar low thermal inertia values may be expected for objects rotating (or that had previously been rotating) close to or at the spin-fission limit. Cohesive forces have already been detected to be preventing the rotational disruption of the NEA (29075) 1950 DA (B. Rozitis et al. 2014; B. Gundlach & J. Blum 2015). The similarity of the grain sizes for these objects, despite their differing spectral classifications (C type for 1996 FG3, E/Xe type for 1998 WT24, S type for Dinkinesh, and E/M type for 1950 DA), suggests that cohesive forces are not preferentially found among any specific regolith composition and should be present across a wide range of asteroid surfaces. Although the presence of cohesive forces does not appear to be composition-dependent, the strength of such forces may still depend on mineralogy and the degree of thermal metamorphism in the regolith material (Y. Nagaashi et al. 2021).

5.3. Surface Roughness

The roughness derived for Dinkinesh of the 35° ± 7° rms slope is widely comparable to a range of atmosphereless bodies across the solar system, although the uncertainty on this value is relatively high (20%), which enables a lot of overlap between bodies. First, it is comparable at the upper range of roughness measurements of the Moon, ~20°–35° (B. Rozitis & S. F. Green 2011; J. L. Bandfield et al. 2015; T. G. Müller et al. 2021). Second, the derived roughness is comparable to that determined for other S-type asteroids such as (65803) Didymos (40° ± 3°; B. Rozitis et al. 2024) and (433) Eros (38° ± 8°; B. Rozitis 2017). Values for the C-type asteroids (101955) Bennu and (162173) Ryugu of 40° ± 2° (B. Rozitis et al. 2020) and 47° ± 5° (Y. Shimaki et al. 2020), respectively, are also comparable at the upper end of the range for Dinkinesh. The nature of the surface roughness on Dinkinesh therefore lies somewhere between that of Bennu and the Moon and is most similar to that of Eros. It is interesting that both the thermal inertia and surface roughness of Dinkinesh match well to Eros, considering the wildly different scales of these bodies (Dinkinesh: $D \sim 700$ m; Eros: $D \sim 17$ km).

This surface roughness is relevant at scales from the thermal skin depth up to the shape facet size (in our downsampled version of the shape model, the facet size is ~27 m). The thermal skin depth is calculated as

$$l = \frac{\Gamma}{\rho C}\sqrt{\frac{P}{2\pi}}, \tag{9}$$

where l is the skin depth, Γ is the thermal inertia, ρ is the bulk density of material, C is the specific heat capacity, and P is the period (in this case, the rotation period to obtain the diurnal skin depth). Using $\Gamma = 91 \pm 24\,\mathrm{J\,m^{-2}\,K^{-1}\,s^{-1/2}}$, $\rho = \sim 2200 \pm 320\,\mathrm{kg\,m^{-3}}$ (F. Preusker et al. 2024), $C = 570\,\mathrm{J\,kg^{-1}\,K^{-1}}$ (based on values for L-chondrites; C. P. Opeil et al. 2010), and $P_{\mathrm{ROT}} = 3.737$ hr (F. Preusker et al. 2024), we derive a diurnal thermal skin depth of $l = 1.08 \pm 0.33$ cm.

5.4. Remaining Sources of Uncertainty

In Section 2, we discussed the potential impact of additional contributions to the measured L'TES radiance spectra by the secondary, Selam. Given the relatively low expected flux contribution, the lack of a shape model for Selam to allow for accurate modeling of its thermal flux, and the requirement to understand the sensitivity variations across the L'TES instrument, this systematic is left uncharacterized and is instead handled by the presence of the scale factors in the fitting process.

One additional source of systematic error is the contribution from Dinkinesh's surface that was not visible to the L'LORRI instrument but is detected in the L'TES data (as there is nightside contribution to the flux for thermal inertia values greater than $0\,\mathrm{J\,m^{-2}\,K^{-1}\,s^{-1/2}}$). The shape model, presented in F. Preusker et al. (2024), has been created using both L'LORRI close approach imaging data and postencounter light curves. The inclusion of the light-curve data enabled asteroid surfaces not observable by L'LORRI to be described at low resolution, allowing L'TES data to be used at higher phase angles. Figure 8 is an animation showing a view of the geometry of the flyby with simulations of the illumination and surface temperatures visible in the left and right images, respectively. This animation demonstrates that at high phase angles during the approach, a large proportion of the surface area visible to L'TES is on the nightside; therefore, the unknown quality of the shape model in this region may be affecting our model fits. However, the nightside is at a significantly lower temperature and will therefore contribute a smaller proportion of the total flux received at the detector, so this effect may be small. The use of a thermal imager in future missions may limit such systematic issues, although these provide worse spectral coverage (which could hinder determination of thermal inertia).

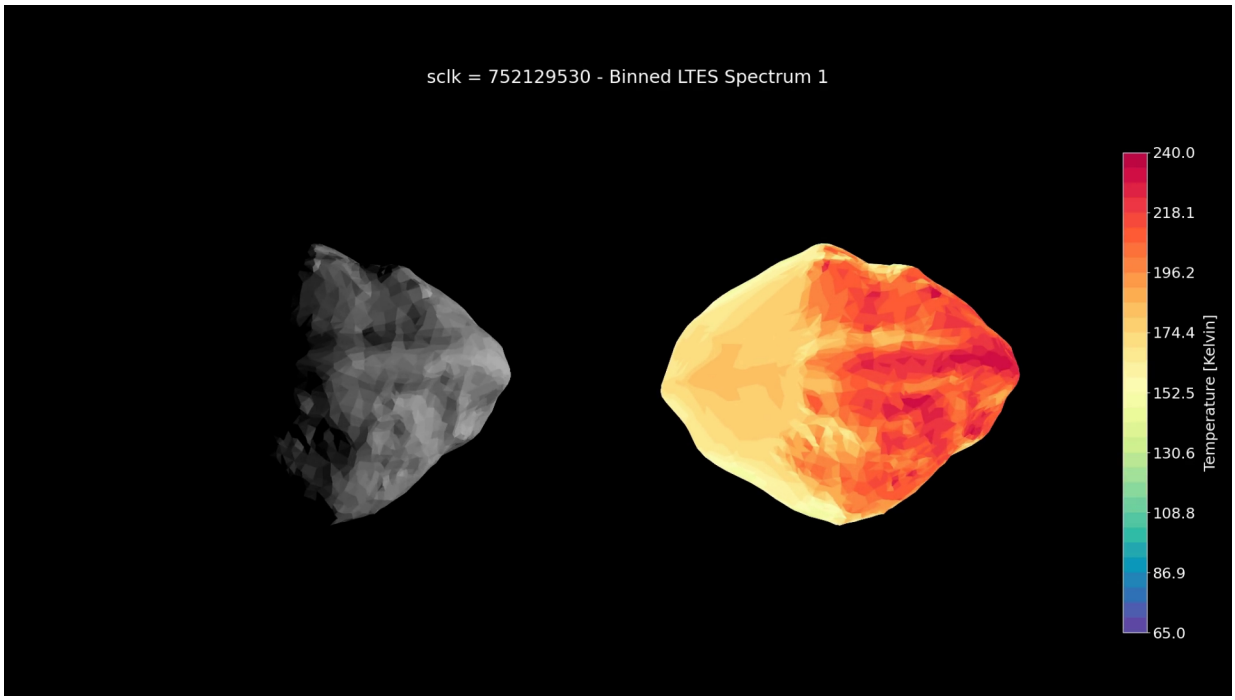

Figure 8. Demonstration of a high phase angle geometry on approach to Dinkinesh where the unlit side (and therefore the side with a lower-quality shape model) comprises a significant proportion of the area of Dinkinesh visible to the L'TES instrument. The unlit side, however, is cooler and therefore contributes less flux to the total received at the detector. The left image shows simulated illumination, mapped onto the downsampled shape model of Dinkinesh discussed earlier. The right image shows the simulated temperature distribution, similarly mapped onto the downsampled shape model. The title in the image indicates where the times correspond to the period of one of our 10 average spectra. An animated version of this figure shows the simulated geometries of the full encounter. The animation shows how the relative geometry of Dinkinesh would have looked from the Lucy spacecraft as the encounter progressed. The speed of the animation decreases from 60× real-time speed to 15× real-time speed during the period covering the analyzed L'TES spectra.
(An animation of this figure is available in the online article.)

6. Summary

In this work, we have provided an overview of the data collected by the L'TES instrument during the Lucy mission flyby of asteroid Dinkinesh. We have applied thermal models, in combination with spin and shape information derived from the L'LORRI instrument, to calculate the thermal inertia of (152830) Dinkinesh as $91 \pm 24\,\mathrm{J\,m^{-2}\,K^{-1}\,s^{-1/2}}$, the regolith grain size as $r = 1.2^{+0.9}_{-0.6}$ mm, and the surface roughness as $35° \pm 7°$ rms slope. The thermal inertia and surface roughness values compare well with other S-type asteroids visited by spacecraft such as (65803) Didymos and (433) Eros. However, the regolith grain size is lower than expected for an object of this size. Similar grain sizes calculated from unresolved telescopic observations for the similarly sized objects (175706) 1996 FG3 (binary) and (33342) 1998 WT24 (close to the spin-fission limit 75 kyr ago) suggest that either cohesive forces are commonly acting to retain fine-grained material on asteroids undergoing material loss due to rotational forces or some other process such as impacts onto secondaries redeposits fines back onto the surface of the primary. However, our data do not allow us to fully distinguish whether the differences in this characteristic grain size could also reflect a difference in the overall particle size distribution instead of a difference in the "average" size.

The flyby of Dinkinesh has enabled lessons to be learned regarding the analysis of L'TES data for the recent (2025 April) flyby of (52246) Donaldjohanson and for the analysis of the Trojans during the remainder of the Lucy mission. The ability to extract useful information when only a fraction of the FOV is filled provides confidence that the data collected during future flybys where the FOV will be filled will produce excellent results and contribute to the interpretation of the regolith properties of the Trojan asteroids observed.

Acknowledgments

The Lucy mission is funded through the NASA Discovery program on contract No. NNM16AA08C. S.L.J. and B.R. were funded by the Science and Technology Facilities Council under grant ST/X001180/1. The authors thank the L'TES team and the entire Lucy mission team and appreciate the hours contributed to discussions by members of the Lucy Surface Composition Working Group. We thank the anonymous reviewers for their insights, which have helped to improve the rigor and quality of the analysis and manuscript. All calibrated L'TES data can be retrieved from the PDS small bodies node at doi:10.26007/83dq-8a53 (P. R. Christensen et al. 2024a). All L'LORRI data can be retrieved from the PDS small bodies node at doi:10.26007/kvc4-2t38 (H. Weaver et al. 2024).

Appendix
ATPM Model Fits to L'TES Data

In Figure A1, the 10 averaged L'TES spectra are shown alongside the homogeneous surface ATPM model fits and single-temperature blackbody fits. In Figure A2, the 10 averaged L'TES spectra are shown alongside the heterogeneous surface ATPM model fits and single-temperature blackbody fits.

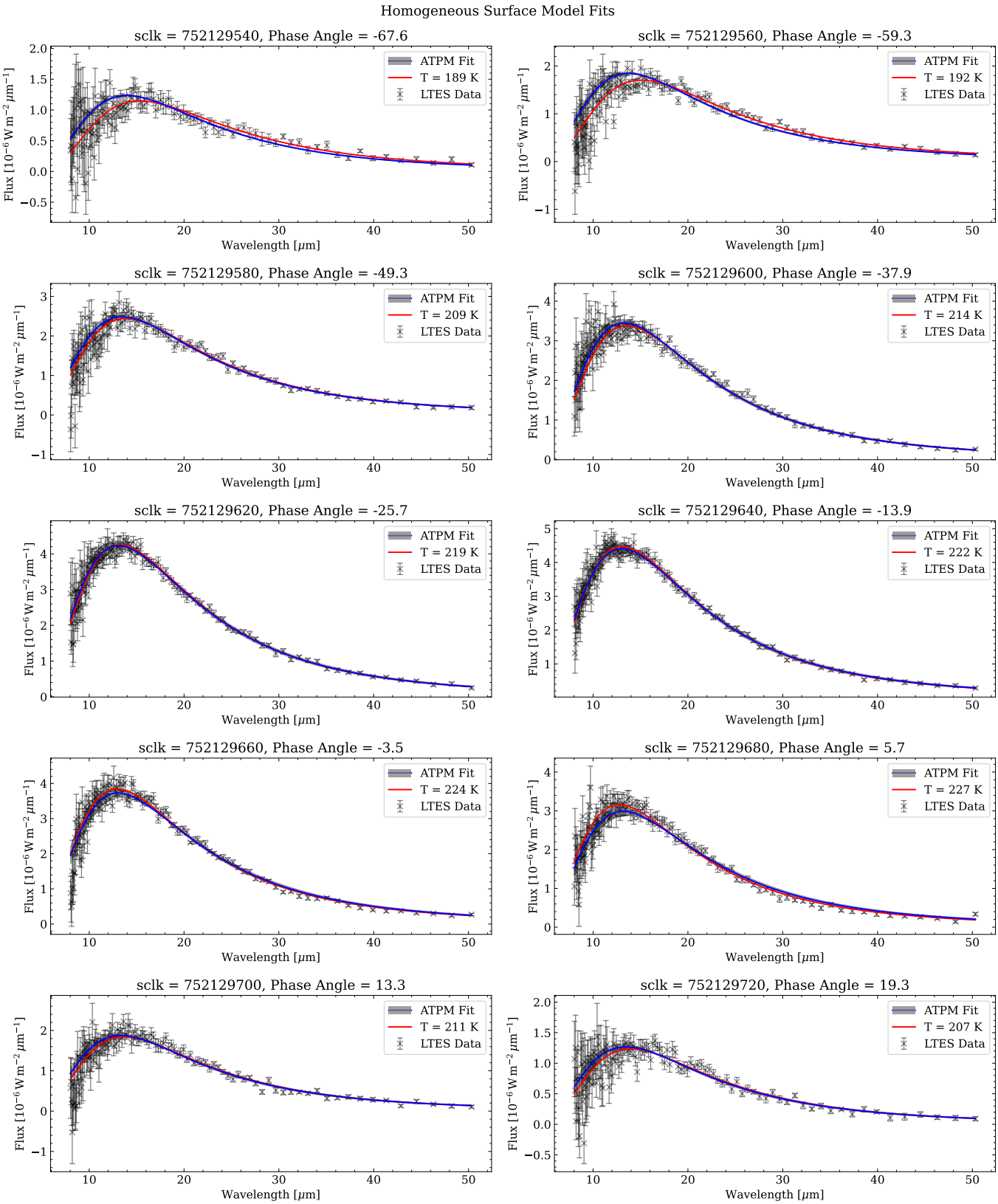

Figure A1 L'TES data binned into 10 spectra (crosses), ATPM homogeneous surface model fits and corresponding uncertainty region (blue lines and shaded areas), and the single-temperature blackbody fit to the data (red lines).

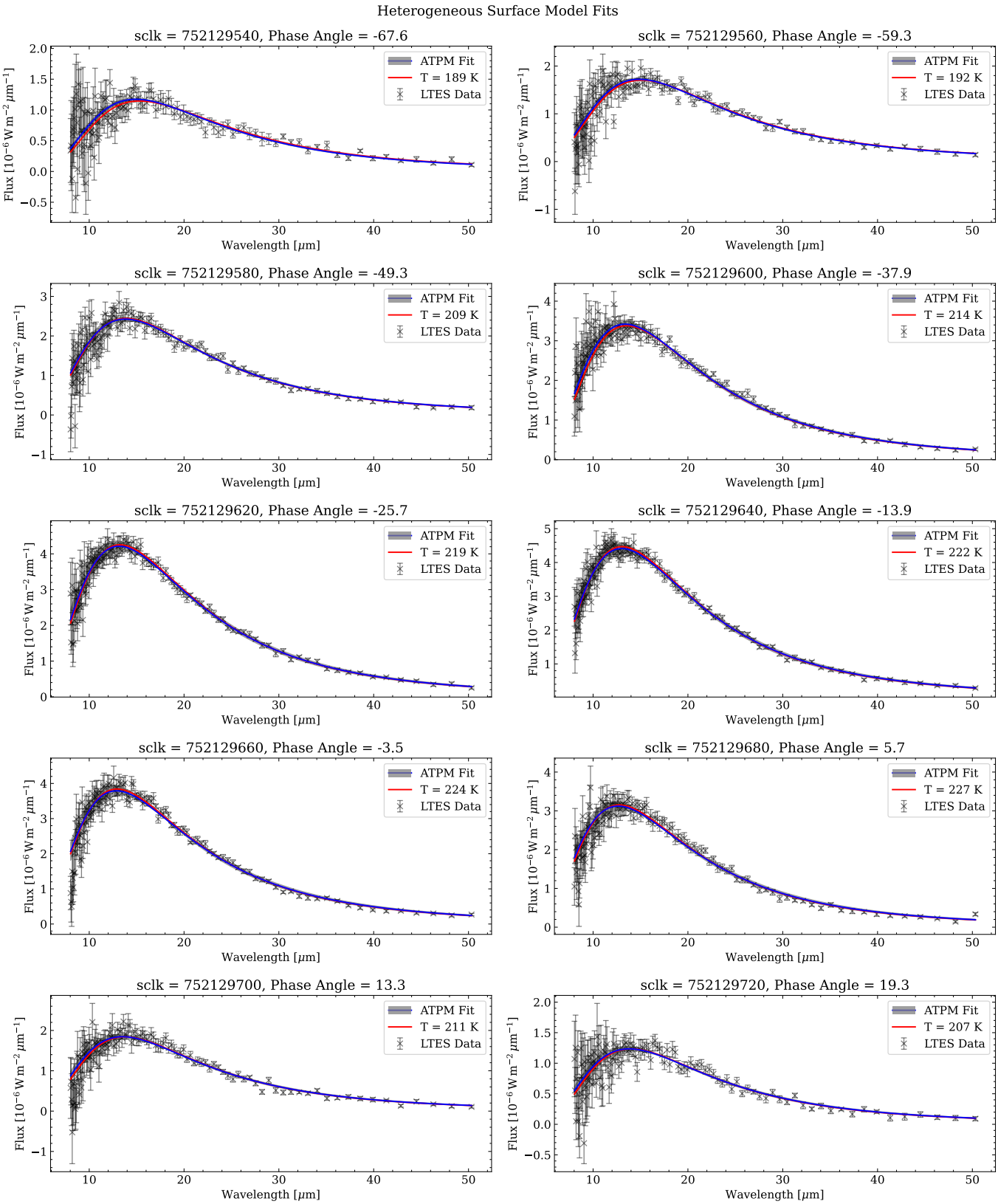

Figure A2 L'TES data binned into 10 spectra (crosses), ATPM heterogeneous surface model fits and corresponding uncertainty region (blue lines and shaded areas), and the single-temperature blackbody fit to the data (red lines).

ORCID iDs

Samuel L. Jackson https://orcid.org/0000-0001-9242-4254
Joshua P. Emery https://orcid.org/0000-0001-9265-9475
Benjamin Rozitis https://orcid.org/0000-0001-9893-241X
Philip R. Christensen https://orcid.org/0000-0001-9625-4723
John R. Spencer https://orcid.org/0000-0003-4452-8109
Stefano Mottola https://orcid.org/0000-0002-0457-3872
Victoria E. Hamilton https://orcid.org/0000-0001-8675-2083
Carly J. A. Howett https://orcid.org/0000-0003-1869-4947
Simone Marchi https://orcid.org/0000-0003-2548-3291
Keith S. Noll https://orcid.org/0000-0002-6013-9384
Harold F. Levison https://orcid.org/0000-0001-5847-8099

References

Alí-Lagoa, V., Lionni, L., Delbo, M., et al. 2014, Thermophysical Properties of Near-Earth Asteroid (341843) 2008 EV_5 from WISE Data, A&A, 561, A45
Bandfield, J. L., Hayne, P. O., Williams, J.-P., Greenhagen, B. T., & Paige, D. A. 2015, Lunar Surface Roughness Derived from LRO Diviner Radiometer Observations, Icar, 248, 357
Barnouin, O., Ballouz, R.-L., Marchi, S., et al. 2024, The Geology and Evolution of the Near-Earth Binary Asteroid System (65803) Didymos, NatCo, 15, 6202
Bolin, B. T., Noll, K. S., Caiazzo, I., Fremling, C., & Binzel, R. P. 2023, Keck and Gemini Spectral Characterization of Lucy Mission Fly-by Target (152830) Dinkinesh, Icar, 400, 115562
Busch, M. W., Benner, L. A. M., Ostro, S. J., et al. 2008, Physical Properties of Near-Earth Asteroid (33342) 1998 WT24, Icar, 195, 614
Chabot, N. L., Rivkin, A. S., Cheng, A. F., et al. 2024, Achievement of the Planetary Defense Investigations of the Double Asteroid Redirection Test (DART) Mission, PSJ, 5, 49
Christensen, P. R., Hamilton, V. E., Anwar, S., Mehall, G. L., & Bowles, H. 2024a, Lucy L'TES Dinkinesh Calibrated Data Collection, NASA Planetary Data System, urn:nasa:pds:lucy.ltes:data_dinkinesh_calibrated::1.0, doi:10.26007/83dq-8a53
Christensen, P. R., Hamilton, V. E., Emery, J. P., et al. 2024c, Lucy Thermal Emission Spectrometer (L'TES) Temperature Observations of Dinkinesh, LPSC, 3040, 1384
Christensen, P. R., Hamilton, V. E., Mehall, G. L., et al. 2018, The OSIRIS-REx Thermal Emission Spectrometer (OTES) Instrument, SSRv, 214, 87
Christensen, P. R., Hamilton, V. E., Mehall, G. L., et al. 2024b, The Lucy Thermal Emission Spectrometer (L'TES) Instrument, SSRv, 220, 1
Cignoni, P., Callieri, M., Corsini, M., et al. 2008, Meshlab: An Open-source Mesh Processing Tool, in Eurographics Italian Chapter Conf., ed. V. Scarano, R. D. Chiara, & U. Erra (Eindhoven: The Eurographics Association)
Delbo, M., Mueller, M., Emery, J. P., Rozitis, B., & Capria, M. T. 2015, Asteroid Thermophysical Modeling, in Asteroids IV, ed. P. Michel, F. E. DeMeo, & W. F. Bottke (Tucson, AZ: Univ. Arizona Press), 107
de León, J., Licandro, J., Pinilla-Alonso, N., et al. 2023, Characterisation of the New Target of the NASA Lucy Mission: Asteroid 152830 Dinkinesh (1999 VD57), A&A, 672, A174
DellaGiustina, D. N., Emery, J. P., Golish, D. R., et al. 2019, Properties of Rubble-pile Asteroid (101955) Bennu from OSIRIS-REx Imaging and Thermal Analysis, NatAs, 3, 341
DellaGiustina, D. N., Nolan, M. C., Polit, A. T., et al. 2023, OSIRIS-APEX: An OSIRIS-REx Extended Mission to Asteroid Apophis, PSJ, 4, 198
Garland, M., & Heckbert, P. S. 1997, Surface Simplification Using Quadric Error Metrics, in Proc. 24th Annual Conf. Computer Graphics and Interactive Techniques, ed. G. S. Owen & T. Whitted (New York: ACM), 209
Gray, Z., Bagnulo, S., Granvik, M., et al. 2024, Polarimetry of Didymos–Dimorphos: Unexpected Long-term Effects of the DART Impact, PSJ, 5, 18
Gundlach, B., & Blum, J. 2012, Outgassing of Icy Bodies in the Solar System—II: Heat Transport in Dry, Porous Surface Dust Layers, Icar, 219, 618
Gundlach, B., & Blum, J. 2013, A New Method to Determine the Grain Size of Planetary Regolith, Icar, 223, 479
Gundlach, B., & Blum, J. 2015, Regolith Grain Size and Cohesive Strength of Near-Earth Asteroid (29075) 1950 DA, Icar, 257, 126
Hanuš, J., Delbo', M., Ďurech, J., & Alí-Lagoa, V. 2018, Thermophysical Modeling of Main-belt Asteroids from WISE Thermal Data, Icar, 309, 297
Jackson, S. L., & Rozitis, B. 2024, Thermophysical Modeling of Eclipse and Occultation Events in Binary Asteroid Systems, MNRAS, 534, 1827
Levison, H. F., Marchi, S., Noll, K. S., et al. 2024, A Contact Binary Satellite of the Asteroid (152830) Dinkinesh, Natur, 629, 1015
Levison, H. F., Olkin, C. B., Noll, K. S., et al. 2021, Lucy Mission to the Trojan Asteroids: Science Goals, PSJ, 2, 171
MacLennan, E. M., & Emery, J. P. 2022, Thermophysical Investigation of Asteroid Surfaces. II. Factors Influencing Grain Size, PSJ, 3, 47
Marchis, F., Enriquez, J. E., Emery, J. P., et al. 2012, Multiple Asteroid Systems: Dimensions and Thermal Properties from Spitzer Space Telescope and Ground-based Observations, Icar, 221, 1130
Michel, P., Küppers, M., Bagatin, A. C., et al. 2022, The ESA Hera Mission: Detailed Characterization of the DART Impact Outcome and of the Binary Asteroid (65803) Didymos, PSJ, 3, 160
Miyamoto, H., Yano, H., Scheeres, D. J., et al. 2007, Regolith Migration and Sorting on Asteroid Itokawa, Sci, 316, 1011
Mottola, S., Denk, T., Marchi, S., et al. 2023, Characterizing Asteroid (152830) Dinkinesh in Preparation for the Encounter with the NASA Lucy Mission: A Photometric Study, MNRAS, 524, L1
Mottola, S., Preusker, F., Weaver, H. A., et al. 2024, Photometric Properties of (152830) Dinkinesh from Disk-resolved Imaging, LPSC, 3040, 2119
Müller, M. M. 2007, PhD thesis, Free Univ. Berlin, Germany
Müller, T. G., Burgdorf, M., Alí-Lagoa, V., Buehler, S. A., & Prange, M. 2021, The Moon at Thermal Infrared Wavelengths: A Benchmark for Asteroid Thermal Models, A&A, 650, A38
Müller, T. G., Hasegawa, S., & Usui, F. 2014, (25143) Itokawa: The Power of Radiometric Techniques for the Interpretation of Remote Thermal Observations in the Light of the Hayabusa Rendezvous Results, PASJ, 66, 52
Nagaashi, Y., Aoki, T., & Nakamura, A. M. 2021, Cohesion of Regolith: Measurements of Meteorite Powders, Icar, 360, 114357
Nakamura, T., Noguchi, T., Tanaka, M., et al. 2011, Itokawa Dust Particles: A Direct Link Between S-type Asteroids and Ordinary Chondrites, Sci, 333, 1113
Olkin, C. B., Levison, H. F., Vincent, M., et al. 2021, Lucy Mission to the Trojan Asteroids: Instrumentation and Encounter Concept of Operations, PSJ, 2, 172
Opeil, C. P., Consolmagno, G. J., & Britt, D. T. 2010, The Thermal Conductivity of Meteorites: New Measurements and Analysis, Icar, 208, 449
Press, W. H., Teukolsky, S. A., Vetterling, W. T., & Flannery, B. P. 2002, Numerical Recipes in C++: The Art of Scientific Computing (Cambridge: Cambridge Univ. Press)
Preusker, F., Mottola, S., Matz, K.-D., et al. 2024, Shape Model of Asteroid (152830) Dinkinesh from Lucy Imagery, EPSC, 17, EPSC2024–963
Rivkin, A. S., Chabot, N. L., Stickle, A. M., et al. 2021, The Double Asteroid Redirection Test (DART): Planetary Defense Investigations and Requirements, PSJ, 2, 173
Rozitis, B. 2017, The Surface Roughness of (433) Eros as Measured by Thermal-infrared Beaming, MNRAS, 464, 915
Rozitis, B., Duddy, S. R., Green, S. F., & Lowry, S. C. 2013, A Thermophysical Analysis of the (1862) Apollo Yarkovsky and YORP Effects, A&A, 555, A20
Rozitis, B., & Green, S. F. 2011, Directional Characteristics of Thermal-infrared Beaming from Atmosphereless Planetary Surfaces—A New Thermophysical Model, MNRAS, 415, 2042
Rozitis, B., & Green, S. F. 2012, The Influence of Rough Surface Thermal-infrared Beaming on the Yarkovsky and YORP Effects, MNRAS, 423, 367
Rozitis, B., & Green, S. F. 2013, The Influence of Global Self-heating on the Yarkovsky and YORP Eeffects, MNRAS, 433, 603
Rozitis, B., Green, S. F., Jackson, S. L., et al. 2024, Pre-impact Thermophysical Properties and the Yarkovsky Effect of NASA DART Target (65803) Didymos, PSJ, 5, 66
Rozitis, B., Green, S. F., MacLennan, E., & Emery, J. P. 2018, Observing the Variation of Asteroid Thermal Inertia with Heliocentric Distance, MNRAS, 477, 1782
Rozitis, B., Maclennan, E., & Emery, J. P. 2014, Cohesive Forces Prevent the Rotational Breakup of Rubble-pile Asteroid (29075) 1950 DA, Natur, 512, 174
Rozitis, B., Ryan, A. J., Emery, J. P., et al. 2020, Asteroid (101955) Bennu's Weak Boulders and Thermally Anomalous Equator, SciA, 6, eabc3699

Rozitis, B., Ryan, A. J., Emery, J. P., et al. 2022, High-resolution Thermophysical Analysis of the OSIRIS-REx Sample Site and Three Other Regions of Interest on Bennu, JGRE, 127, e07153
Ryan, A. J., Rozitis, B., Pino Munoz, D., et al. 2024, Rocks with Extremely Low Thermal Inertia at the OSIRIS-REx Sample Site on Asteroid Bennu, PSJ, 5, 92
Scheeres, D. J., Hartzell, C. M., Sánchez, P., & Swift, M. 2010, Scaling Forces to Asteroid Surfaces: The Role of Cohesion, Icar, 210, 968
Schultz, R. A. 1995, Limits on Strength and Deformation Properties of Jointed Basaltic Rock Masses, RMRE, 28, 1
Shimaki, Y., Senshu, H., Sakatani, N., et al. 2020, Thermophysical Properties of the Surface of Asteroid 162173 Ryugu: Infrared Observations and Thermal Inertia Mapping, Icar, 348, 113835
Spencer, J. R., Bell, J. F., Christensen, P. R., et al. 2024, The First Lucy Earth Flyby (EGA1), SSRv, 220, 3
Sugita, S., Honda, R., Morota, T., et al. 2019, The Geomorphology, Color, and Thermal Properties of Ryugu: Implications for Parent-body Processes, Sci, 364, eaaw0422
Weaver, H., Dello Russo, N., Barnouin, O., Taylor, H., & Spencer, J. 2024, Lucy L'LORRI Dinkinesh Partially Processed Data Collection, NASA Planetary Data System, urn:nasa:pds:lucy.llorri:data_dinkinesh_partially_processed::1.0, doi:10.26007/kvc4-2t38
Weaver, H. A., Wilson, J. P., Conard, S. J., et al. 2023, The Lucy Long Range Reconnaissance Imager (L'LORRI), SSRv, 219, 82
Wolters, S. D., Rozitis, B., Duddy, S. R., et al. 2011, Physical Characterization of Low Delta-V Asteroid (175706) 1996 FG3, MNRAS, 418, 1246
Yu, L.-L., Ji, J., & Wang, S. 2014, Shape, Thermal and Surface Properties Determination of a Candidate Spacecraft Target Asteroid (175706) 1996 FG3, MNRAS, 439, 3357